

Distributions and correlation properties of offshore wind speeds and wind speed increments

So-Kumnet Sim,^{1,*} Philipp Maass,^{2,†} and H. Eduardo Roman^{3,‡}

¹*Universität Osnabrück, Fachbereich Mathematik/Informatik/Physik, Institut für Physik, Barbarastraße 7, D-49076 Osnabrück, Germany*

²*Universität Osnabrück, Fachbereich Mathematik/Informatik/Physik, Institut für Physik, Barbarastraße 7, D-49076 Osnabrück, Germany*

³*Department of Physics, University of Milano-Bicocca, Piazza della Scienza 3, 20126 Milano, Italy*

(Dated: July 17, 2024, revised October 18, 2024)

We determine distributions and correlation properties of offshore wind speeds and wind speed increments by analyzing wind data sampled with a resolution of one second for 20 months at different heights above sea level in the North Sea. Distributions of horizontal wind speeds can be fitted to Weibull distributions with shape and scale parameters varying weakly with the vertical height separation. Kullback-Leibler divergences between distributions at different heights change with the squared logarithm of the height ratio. Cross-correlations between time derivatives of wind speeds are long-term anticorrelated, and the even parts of their correlation functions satisfy sum rules. Distributions of horizontal wind speed increments change from a tent-like shape to a Gaussian with rising increment lag. A surprising peak occurs in the left tail of the increment distributions for lags in a range 10 – 200 km after applying the Taylor’s hypothesis locally to transform time lags into distances. The peak is decisive in order to obtain an expected and observed linear scaling of third-order structure functions with distance. This suggests that it is an intrinsic feature of atmospheric turbulence.

I. INTRODUCTION

Detailed investigations of wind features are important for testing and further developing theories of atmospheric turbulence. Due to ongoing improvements of measurement techniques [1, 2] and increasing amount of available data, new insights are obtained by analyzing statistical properties of wind speeds over large time and length scales covering many orders of magnitude [3, 4]. Better knowledge of wind properties is of high current interest also for applications, as, for example, for harvesting wind energy [5], or for controlling pollutant dispersion in urban areas [6, 7]. This includes improved forecasting of wind speeds [8–11] and a better understanding of wake effects [12–15]. In addition, spatial correlations on scales of several hundred meters are relevant for mechanical stabilities and performances of wind turbines with steadily growing size [15–17].

Stationary distributions of wind speeds u are commonly described by the Weibull distribution, where its shape and scale parameters vary with location and season [18–20]. Distributions of wind speed increments $\Delta_\tau u = u(t) - u(t - \tau)$ in a time interval τ change in shape strongly with τ . For small lags τ , they decay exponentially for both negative and positive $\Delta_\tau u$, corresponding to a tent-like form in a linear-log representation [21–23]. This implies a nonlinear dependence of their moments with respect to the moment order, a behavior already considered by Kolmogorov in turbulent flows [24] and often referred to as intermittency [25–28]. It is commonly believed that the nonlinear variation of the moments with their order is universal. Different suggestions have been made to describe it [22, 24, 29]. The intermittent features of wind speeds are transferred to wind power feed-in to electricity grids, on the level of both a single wind turbine and an entire wind farm [23].

As the lag τ increases, the shape of increment distributions changes towards that of a Gaussian, with the kurtosis becoming three when τ exceeds one or several days. It was suggested [21] that the probability density of wind speed increments conditioned on the mean wind speed is given by a linear weighting of Gaussian distributions with log-normally distributed standard deviations. By weighting with the Weibull distribution, the unconditioned probability density of wind speeds is obtained. To account for the shape variation of the increment distribution, the parameters of the log-normal distribution are considered to depend on τ [21].

In a complementary approach, commonly referred to as extended self-similarity (ESS) method [30], the moments of absolute values of wind velocity increments are considered [31]. This approach is based on an exact result from the

* ssim@uos.de

† maass@uos.de

‡ hector.roman@unimib.it

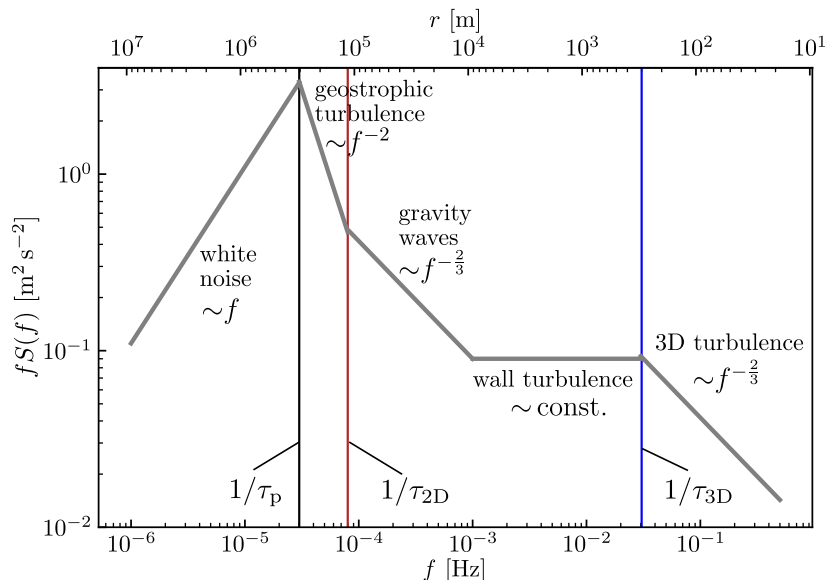


FIG. 1. Schematic sketch of the weighted power spectrum $fS(f)$ of offshore wind speed fluctuations. The upper x -axis shows distances corresponding to the frequencies f when using the Taylor's hypothesis, i.e. that wind speeds passing a point at a time difference τ correspond to wind speeds at a distance given by the mean wind speed multiplied by τ . For real data, see Ref. [4].

theory of three-dimensional (3D) isotropic turbulence for the third-order moment of spatial velocity increments (third-order structure function) and the assumption that this moment is approximately equal to the third-order moment of absolute values of spatial velocity increments. It was pointed out that a lack of 3D isotropy in the turbulent flow, as it is present for near-surface wind flows, narrows the applicability of the ESS method [32]. Nevertheless, studies of measured and model-generated time series of wind speeds showed that the ESS method is useful, with the remarkable result that the scaling of moments with their order is close to that found in isotropic 3D turbulence [33, 34]. In a further application of the ESS method to wind speeds measured at different sites in the Netherlands, a universal intermittent behavior was reported [35]. Applications of the ESS method to other geological and geophysical phenomena revealed similar results as for wind [36]. In an earlier study, downward cascades of turbulent atmospheric flows were shown to be reflected in scaling features of spatial rainfall and river flow distributions [37–41]. Sufficient conditions for the applicability of the ESS methods to dynamical systems in general were derived in [42].

On land, correlation functions of wind speeds show pronounced daily oscillations [43], and their properties depend on the local topography [44, 45]. They are influenced, for example, by buildings [46] and mountains [47]. For offshore wind, daily oscillations are not significant in correlation functions or spectral analysis [3], and the fluctuation properties exhibit generic statistical features. In a recent study of power spectra $S(f)$, distinct frequency regimes were identified displaying characteristic behaviors in agreement with predictions from theories of atmospheric turbulence [4]. These frequency regimes correspond to time regimes, which in turn are reflected in spatial domains when applying the Taylor's hypothesis [48].

The distinct frequency regimes can be well identified by looking at the frequency-weighted spectrum, $fS(f)$, which is presented schematically in Fig. 1 based on results obtained at the measurement height $h = 90$ m [4]. At a frequency $1/\tau_p \sim 3 \times 10^{-5}$ Hz, a peak appears which originates from the motion of low and high-pressure areas in the atmosphere with typical spatial extent of a few thousand kilometers. This peak is also seen in spatial wind speed correlations obtained from aircraft measurements [49, 50].

For frequencies below $1/\tau_p$, the frequency-weighted power spectrum fS increases linearly with f , corresponding to a constant in the power spectrum $S(f)$. Because the analysis for the lowest frequencies was carried out by analyzing ten-minute averages of wind speeds sampled over 15 years, we are confident that the constant $S(f)$ is not due to temporal aliasing effects. Spatial aliasing effects resulting from velocity components orthogonal to the mean flow, however, cannot be ruled out as a possible cause [51, 52]. Alternatively, the constant low-frequency spectrum can reflect white noise behavior due to uncorrelated wind speed fluctuations on time scales larger than τ_p . We believe that this is indeed the case. Further studies would be desirable to clarify this point.

For frequencies above $1/\tau_p$, different physical mechanisms lead to correlations between wind speed fluctuations. They govern the spectral behavior in distinct regimes: below a frequency $1/\tau_{2D} \simeq 8 \times 10^{-5}$ Hz, $fS \sim f^{-2}$, due to an enstrophy cascade in two-dimensional geostrophic turbulence [53]. Above $1/\tau_{2D}$, a regime is dominated by

three-dimensional turbulence induced by gravity waves, where $fS \sim f^{-2/3}$ occurs [54, 55]. At higher frequencies, this regime is followed by one referred to as wall turbulence regime, $fS \sim \text{const.}$, where the air flow is strongly affected by the Earth's surface [56, 57]. Depending on the height h of the wind speed measurement above the sea level, the wall turbulence regime terminates at a frequency $1/\tau_{3D} \sim \bar{v}/h$, where \bar{v} is the mean wind speed. For instance, at $h = 100$ m, we have $1/\tau_{3D} \sim 3 \times 10^{-2}$ Hz. For frequencies above $1/\tau_{3D}$, the spectrum is reflecting isotropic 3D turbulence in accordance with Kolmogorov's celebrated law, $S(f) \sim f^{-5/3}$ [58], i.e. $fS \sim f^{-2/3}$.

Regarding offshore wind data, previous studies have addressed cross-correlations between equal-time horizontal wind speeds at different laterally separated points on the Earth's surface. The cross-correlations were found to decay exponentially for distances in the range 4-600 km, and to stay approximately constant beyond 600 km [59]. In the range 2-12 km, the coherence function also decays exponentially with distance [60].

Measurements performed at a station located at the western tip of the island Frøya in Norway provided information about cross-correlations between horizontal wind speeds in both horizontal and vertical directions to the Earth's surface [61]. For the horizontal direction, the cross-correlation coefficient between equal-time horizontal wind velocities was found to increase with height for velocity components parallel and perpendicular to the mean wind flow. For the vertical direction, the cross-correlation turned out to decay slower with the separation distance if the mean wind speed becomes higher.

In this work, we investigate distribution functions of wind speeds and their increments, on different times scales, as well as time correlation functions between the respective quantities. In particular, we analyze cross-correlations between points separated by a vertical distance Δh .

II. WIND SPEED DATA FROM FINO1

Wind speeds were measured at the FINO1 platform in the North Sea, which is located about 45 km north of the island Borkum [62], see Fig. 2. The wind speed data were sampled by three-cup anemometers over 20 months, from September 2015 to April 2017, for eight different heights h between 30 m and 100 m. The time resolution is $\Delta t = 1$ s, yielding time series with $N \cong 5 \times 10^7$ wind speeds for each height. Because a lightning rod can influence the measurement at $h = 100$ m, we exclude the corresponding data from our analysis.

The time series of wind speeds contain missing values, with the fraction of these values being less than 1% for all heights. For the quantities analyzed in this work, we have checked that no special treatment was necessary for interpolating missing values. When calculating any averaged quantity, results obtained for different interpolation schemes did not differ significantly from those obtained when omitting the missing values.

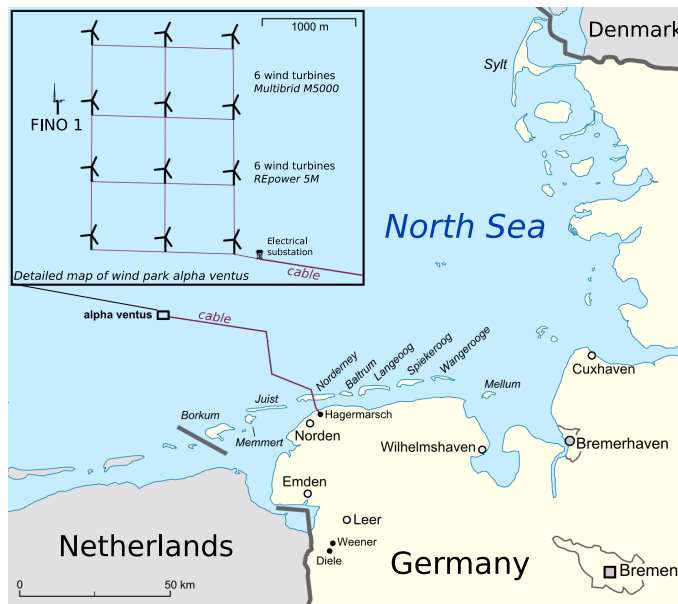


FIG. 2. Location of the FINO1 measurement mast in the North Sea. It is situated near the wind farm “alpha ventus”, approximately 45 km north of the island of Borkum. The figure is a modified version of the map [Wind park alpha ventus](#) from Lencer (CC BY-SA 3.0).

Due to the lack of simultaneous data for wind directions and wind speeds, we cannot perform an analysis separately for different wind directions. The prevailing wind direction at the FINO1 platform is from the west, corresponding to an onshore flow direction [63]. We thus expect that our findings are not significantly affected by wind flows from land. We would also like to note that variations in stratification [64–67] can impact our analysis.

III. THEORETICAL METHODS AND ANALYSIS

A. Distributions of horizontal wind speeds at different heights

PDFs of wind speeds are commonly described by the Weibull distribution [20, 68–71]

$$\psi(u) = \frac{k}{\lambda} \left(\frac{u}{\lambda}\right)^{k-1} e^{-\left(\frac{u}{\lambda}\right)^k} \quad (1)$$

with λ the scale and k the shape parameter. These parameters are estimated by a nonlinear fit of Eq. (1) to the PDF obtained from the wind speed data, where we have used an equidistant binning of the wind speeds with bin sizes in the range 0.42 – 0.52 m/s.

According to the Weibull distribution, the relative standard deviation of wind speeds, also referred to as turbulence intensity, is independent of the scale parameter:

$$\frac{\sigma_u}{\bar{u}} = \sqrt{\frac{\Gamma^2(1 + 1/k)}{\Gamma(1 + 2/k)} - 1}. \quad (2)$$

Here, $\Gamma(\cdot)$ is the Gamma function, and \bar{u} and σ_u are the mean and standard deviation of $\psi(u)$.

To quantify the difference between wind speed distributions $\psi(u; h_1)$ and $\psi(u; h_2)$ at two different heights h_1 and h_2 , we make use of the Kullback-Leibler divergence [72, 73]

$$\begin{aligned} \mathcal{D}[\psi(u; h_1), \psi(u; h_2)] &= \int_0^\infty du \psi(u; h_1) \log \frac{\psi(u; h_1)}{\psi(u; h_2)} \\ &= \log \left(\frac{k_1 \lambda_2^{k_2}}{k_2 \lambda_1^{k_1}} \right) + (k_1 - k_2) \left(\log \lambda_1 - \frac{\gamma}{k_1} \right) + \left[\left(\frac{\lambda_1}{\lambda_2} \right)^{k_2} \Gamma \left(\frac{k_2}{k_1} + 1 \right) - 1 \right], \end{aligned} \quad (3)$$

where γ is the Euler-Mascheroni constant, and k_j and λ_j are the shape and scale parameters of $\psi(u)$ at height h_j . Specifically, we consider the symmetrized Kullback-Leibler (or Jeffrey) divergence,

$$\begin{aligned} D_{\text{KL}}(h_1, h_2) &= \frac{1}{2} (\mathcal{D}[\psi(u; h_1), \psi(u; h_2)] + \mathcal{D}[\psi(u; h_2), \psi(u; h_1)]) \\ &= \frac{1}{2} \log \left[\left(\frac{\lambda_1}{\lambda_2} \right)^{k_1} \left(\frac{\lambda_2}{\lambda_1} \right)^{k_2} \right] + \frac{\gamma}{2} \left(\frac{k_1}{k_2} + \frac{k_2}{k_1} \right) - \gamma - 1 \\ &\quad + \frac{1}{2} \left(\frac{\lambda_1}{\lambda_2} \right)^{k_2} \Gamma \left(\frac{k_2}{k_1} + 1 \right) + \frac{1}{2} \left(\frac{\lambda_2}{\lambda_1} \right)^{k_1} \Gamma \left(\frac{k_1}{k_2} + 1 \right). \end{aligned} \quad (4)$$

B. Temporal cross-correlations of wind speeds and wind speed increments at different heights

Temporal cross-correlations between fluctuations of a quantity $X(t, h_1)$ at height h_1 and $X(t, h_2)$ at height h_2 are investigated based on the normalized cross-correlation function

$$C_X(t; h_1, h_2) = \frac{\langle [X(t', h_1) - \bar{X}(h_1)][X(t' + t, h_2) - \bar{X}(h_2)] \rangle_{t'}}{\sigma_X(h_1)\sigma_X(h_2)} \quad (5)$$

where $\langle \dots \rangle_{t'}$ denotes an average over t' , and $\bar{X}(h) = \langle X(t, h) \rangle_t$ and $\sigma_X(h) = [\langle X^2(t, h) \rangle_t - \langle X(t, h) \rangle_t^2]^{1/2}$ are the mean and standard deviation of X at height h , respectively. For $t = 0$, these cross-correlation functions equal Pearson correlation coefficients between equal-time fluctuations of X at different heights. For $h_1 = h_2 = h$, $C_X(t; h, h)$ is the

normalized autocorrelation function of X at height h . It holds $|C_X(t; h, h)| \leq C_X(0; h, h) = 1$ and $|C_X(t; h_1, h_2)| \leq 1$ for $h_1 \neq h_2$.

We study cross-correlations of both the wind speeds $[X(t, h) = u(t, h)]$ and of their time derivatives $\partial_t u(t, h) \cong u(t + \Delta t, h) - u(t, h)$ $[X(t, h) = u(t + \Delta t, h) - u(t, h), \Delta t = 1\text{s}]$, i.e. horizontal wind accelerations. In power spectra of the offshore wind speeds, we have not seen any signatures of diurnal and annual variations [4]. Diurnal variations in near-surface marine wind are mainly observed when it flows in offshore direction [74], while the wind at the FINO1 platform flows primarily from the west in onshore direction [63]. Annual variations show up as sharp peak in the power spectrum of wind speeds when analyzing 10-minutes averaged wind speed data sampled over 20 months, but it was found also that these do not significantly affect the correlation properties of the wind speed on time scales of 20 months.

We thus regard the wind speed as a stationary process in our correlation analysis. When decomposing the correlations functions into their even and odd parts, i.e. $C_X(t; h_1, h_2) = C_X^+(t; h_1, h_2) + C_X^-(t; h_1, h_2)$ with

$$C_X^\pm(t; h_1, h_2) = \frac{1}{2} [C_X(t; h_1, h_2) \pm C_X(-t; h_1, h_2)] , \quad (6)$$

the even parts should fulfill the relation

$$C_u^+(t; h_1, h_2) = C_u^+(0; h_1, h_2) - \frac{\sigma_{\partial_t u}(h_1)\sigma_{\partial_t u}(h_2)}{\sigma_u(h_1)\sigma_u(h_2)} \int_0^t dt' (t - t') C_{\partial_t u}^+(t'; h_1, h_2) , \quad (7)$$

and $C_{\partial_t u}^+(t; h_1, h_2)$ the two sum rules

$$\int_0^\infty dt C_{\partial_t u}^+(t; h_1, h_2) = 0 , \quad (8)$$

$$\int_0^\infty dt C_{\partial_t u}^+(t; h_1, h_2) t = - \frac{\text{cov}[u(t, h_1)u(t, h_2)]}{\sigma_{\partial_t u}(h_1)\sigma_{\partial_t u}(h_2)} . \quad (9)$$

Here, $\text{cov}[u(t, h_1), u(t, h_2)] = \langle [u(t, h_1) - \bar{u}(h_1)][u(t, h_2) - \bar{u}(h_2)] \rangle$ is the covariance between equal-time wind speeds at heights h_1 and h_2 , which becomes the variance $\sigma_u^2(h)$ for $h_1 = h_2 = h$. Note that the auto-correlation functions are even functions of time, $C_X^-(t; h, h) = 0$.

Equations (7)-(9) can be derived by using

$$u(t, h) - u(0, h) = \int_0^t dt' \frac{\partial u(t', h)}{\partial t'} , \quad (10)$$

and by taking into account that $\partial_t u(t, h)$ is a stationary process. It thus holds

$$\begin{aligned} \langle [u(t, h_1) - u(0, h_1)][u(t, h_2) - u(0, h_2)] \rangle &= \int_0^t dt_1 \int_0^t dt_2 \left\langle \frac{\partial u(t_1, h_1)}{\partial t_1} \frac{\partial u(t_2, h_2)}{\partial t_2} \right\rangle \\ &= \sigma_{\partial_t u}(h_1)\sigma_{\partial_t u}(h_2) \int_0^t dt_1 \int_0^t dt_2 C_{\partial_t u}(t_1 - t_2; h_1, h_2) \\ &= 2\sigma_{\partial_t u}(h_1)\sigma_{\partial_t u}(h_2) \left[t \int_0^t dt' C_{\partial_t u}^+(t'; h_1, h_2) - \int_0^t dt' t' C_{\partial_t u}^+(t'; h_1, h_2) \right] . \end{aligned} \quad (11)$$

The simplification of the double integral of $C_{\partial_t u}(t_1 - t_2; h_1, h_2)$ over t_1 and t_2 to the single integrals in the last line is possible due to the fact that the integrand is a function of $(t_1 - t_2)$ only.

Defining $\delta u(t, h) = u(t, h) - \bar{u}(h)$, the left-hand side of Eq. (11) can be rewritten as

$$\begin{aligned} & \langle [u(t, h_1) - u(0, h_1)][u(t, h_2) - u(0, h_2)] \rangle \\ &= \langle [\delta u(t, h_1) - \delta u(0, h_1)][\delta u(t, h_2) - \delta u(0, h_2)] \rangle \\ &= 2\langle \delta u(0, h_1)\delta u(0, h_2) \rangle - [\langle \delta u(t, h_1)\delta u(0, h_2) \rangle + \langle \delta u(0, h_1)\delta u(t, h_2) \rangle] \\ &= 2\text{cov}[u(t, h_1), u(t, h_2)] - 2\sigma_u(h_1)\sigma_u(h_2)C_u^+(t; h_1, h_2). \end{aligned} \quad (12)$$

Equating this with the right-hand side of Eq. (11) yields Eq. (7).

When considering the limit $t \rightarrow \infty$ in Eq. (11), the left-hand side becomes two times the covariance $\text{cov}[u(t, h_1), u(t, h_2)]$. Accordingly, the first integral in the square bracket in Eq. (11) must vanish, which yields Eq. (8), and the remaining second integral in Eq. (11) must satisfy Eq. (9).

To quantify the correlation between wind speed increments

$$\Delta_\tau u(t, h) = u(t, h) - u(t - \tau, h), \quad (13)$$

for time lags $\tau > 1$ s at different heights, we calculate the Pearson correlation coefficient

$$\rho(\tau; h_1, h_2) = C_{\Delta_\tau u}(0; h_1, h_2) = \frac{\langle \Delta_\tau u(t, h_1)\Delta_\tau u(t, h_2) \rangle}{\sqrt{\langle \Delta_\tau u^2(t, h_1) \rangle \langle \Delta_\tau u^2(t, h_2) \rangle}}. \quad (14)$$

C. Detrended fluctuation analysis of differences between wind speeds in vertical direction

To study how differences

$$\Delta u_{h_1, h_2}(t) = u(t, h_1) - u(t, h_2) \quad (15)$$

between horizontal wind speeds at different heights h_1 and h_2 fluctuate in time, we apply the detrended fluctuation analysis (DFA) [75]. This is a valuable method in particular in the presence of long-range power-law correlations.

In the DFA, the $\Delta u_{h_1, h_2}(t)$ are considered as positions of a random walk. A sub- or superlinear power-law scaling of its mean squared displacement with time signals long-range power-law decays of the correlation function $C(t; \Delta u_{h_1, h_2}, \Delta u_{h_1, h_2})$. To uncover such correlations clearly, the DFA includes a detrending due to local biases.

Specifically, we define a profile of the detrended random walk in a time window t by

$$R_{h_1, h_2}(t') = \sum_{t''=1}^{t'} \Delta u_{h_1, h_2}(t'') - \frac{t'}{t} \sum_{t''=1}^t \Delta u_{h_1, h_2}(t''), \quad 1 \leq t' \leq t, \quad (16)$$

where the second term removes a linear bias in the time window. Note that $R_{h_1, h_2}(0) = R_{h_1, h_2}(t) = 0$. The time series of total duration T is divided into $M = \lfloor T/t \rfloor$ time windows of size t , where $\lfloor x \rfloor$ is the largest integer smaller than x . The mean of the profile in the m th window is

$$\bar{R}_{h_1, h_2}(m) = \frac{1}{t} \sum_{t'=1}^t R_{h_1, h_2}[(m-1)t + t'], \quad m = 1, \dots, M. \quad (17)$$

It is a measure of the mean of detrended wind speed differences in the m th window on time scale t . Differently speaking, it is the m th position of the detrended random walk, when it is coarse-grained on time scale t . The variance

$$F_{h_1, h_2}(t) = F_{h_2, h_1}(t) = \frac{1}{M-1} \sum_{m=1}^{M-1} [\bar{R}_{h_1, h_2}(m+1) - \bar{R}_{h_1, h_2}(m)]^2 \quad (18)$$

of the displacements $\bar{R}_{h_1, h_2}(m+1) - \bar{R}_{h_1, h_2}(m)$ of this random walk quantifies the strength of fluctuations of $\Delta u_{h_1, h_2}(t)$ on time scale t . It is called the fluctuation function in the DFA.

For power-law behavior

$$F_{h_1, h_2}(t) \sim t^H, \quad (19)$$

at long times with $0 < H < 1$, H is commonly referred to as the Hurst exponent. Values $1/2 < H < 1$ correspond to a long-range power-law decay $\sim t^{2H-2}$ of the autocorrelation function $\langle \partial_t \Delta u_{h_1, h_2}(t') \partial_t \Delta u_{h_1, h_2}(t' + t) \rangle_{t'}$.

D. Distribution functions of horizontal wind speed increments at different Taylor distances

For analyzing distributions of horizontal wind speed increments at a constant height, we make use of the Taylor's hypothesis. Applying it requires sufficiently low turbulence intensities σ_u/\bar{u} . For our data, $\sigma_u/\bar{u} = 0.52$, which is at the limit where the hypothesis was found to break down [76]. Indeed, in a previous analysis of the offshore wind data [4] we have seen that Taylor's hypothesis does not give reliable results when applying it with the mean wind speed calculated from the whole time series.

However, reliable results were obtained if the hypothesis was applied locally: the scaling of structure functions agrees well with theoretical predictions for atmospheric turbulence, and with results obtained from an analysis of wind fields measured by aircraft [77]. Here we also apply the Taylor's hypothesis locally to convert data from the time to the spatial domain.

In this method, we first calculate the average wind speed $\bar{u}_{t, t+\tau}$ in the interval $[t, t + \tau]$. The time interval is then converted into a distance $r_{t, t+\tau} = \bar{u}_{t, t+\tau} \tau$, which we refer to as the Taylor distance for time lag τ at time t . For each pair of times $(t, t + \tau)$, we calculate the distance $r = r_{t, t+\tau}$, and the corresponding wind speed increment $\Delta_r u \equiv u_t - u_{t+\tau}$. The $\Delta_r u$ are then grouped with respect to equally spaced Taylor distances r on a logarithmic scale. The j th group contains all wind speed increments for r lying in the interval $[r_j^-, r_{j+1}^-]$, $j = 0, 1, \dots, j_{\max}$, where $r_j^- = r_0 10^{j/10}$ with $r_0 = 1$ m. The value of r assigned to the j th group is the geometric mean $r_j = (r_j^- r_{j+1}^-)^{1/2}$, corresponding to the arithmetic mean of logarithms, $\ln r_j = (\ln r_j^- + \ln r_{j+1}^-)/2$. For each r_j , the wind speed increments $\Delta_r u$ are sampled in small bins $\Delta_r u$ to obtain the PDFs $p_r(\Delta_r u)$.

E. Scaling behavior of moments of horizontal wind speed increment distributions

Characteristic turbulence features can be identified through the scaling behavior of structure functions, which are moments of $p_r(\Delta_r u)$ of order q :

$$D_q(r) = \langle (\Delta_r u)^q \rangle. \quad (20)$$

The third-order structure function D_3 is expected to follow known behaviors in certain distance or time regimes. In the regime of 3D isotropic turbulence, D_3 is negative, proportional to the energy dissipation rate ϵ and grows linearly with r [78, 79]:

$$D_3(r) = -\frac{4}{5}\epsilon r. \quad (21)$$

Here, ϵ is the energy dissipation rate. For gravity-wave induced turbulence, Coriolis forces cannot be neglected, which leads to a modified amplitude in the linear scaling of the third-order structure function [80]:

$$D_3(r) = -2\epsilon r. \quad (22)$$

In quasi-2D geostrophic turbulence, D_3 is positive and scales as

$$D_3(r) = \frac{1}{4}\eta r^3, \quad (23)$$

where η is the enstrophy dissipation rate [54, 80–83]. In the regime of wall turbulence, a simple scaling of D_3 with r is not expected but measurements have shown that D_3 is negative in general [4].

To examine intermittency in the regime of 3D isotropic turbulence, we consider absolute values of wind speed increments. The corresponding moments are denoted as $\tilde{D}_q(r)$ to distinguish them from the ones in Eq. (20):

$$\tilde{D}_q(r) = \langle |\Delta_r u|^q \rangle. \quad (24)$$

As $D_3 \sim -r$ in the considered regime, one can expect that $\tilde{D}_3 \sim r$ also, which is indeed obtained. As for other moments, a self-similar structure of the turbulent field [58] would imply a monofractal behavior $\tilde{D}_q \sim \tilde{D}_3^{q/3} \sim r^{q/3}$.

However, due to intermittent behavior,

$$\tilde{D}_q(r) \sim r^{\zeta(q)}, \quad (25)$$

or

$$\tilde{D}_q(r) \sim \tilde{D}_3^{\zeta(q)}, \quad (26)$$

where $\zeta(q)$ is a nonlinear function of q with $\zeta(3) = 1$. Deviations from the linear dependence $\zeta(q) = q/3$ give insight into the multifractal scaling due to intermittency. Based on a turbulent cascade model with log-normally distributed energy transfer rates, Kolmogorov [24] derived

$$\zeta(q) = \frac{q}{3} - \frac{\mu}{18}q(q-3), \quad (27)$$

where the intermittency correction μ lies in the range $0.2 - 0.5$ [84, 85]. Assuming high velocity fluctuations on small spatial scales, another nonlinear behavior

$$\zeta(q) = \frac{q}{9} + 2 \left[1 - \left(\frac{2}{3} \right)^{q/3} \right], \quad (28)$$

was proposed by She and Leveque [29]. Several other functions $\zeta(q)$ were suggested in the literature [86, 87]. We will determine exponents $\zeta(q)$ by fitting power laws to data of \tilde{D}_q vs. r [Eq. (25)] and of \tilde{D}_q vs. \tilde{D}_3 [Eq. (26)] in the inertial range of 3D isotropic turbulence. The fitting to data of \tilde{D}_q vs. \tilde{D}_3 corresponds to the ESS analysis [30]. Exponents $\zeta(q)$ obtained from the power-law fits are checked against the theoretical predictions (27) and (28).

IV. RESULTS

We discuss our results according to the subsectioning in the Theoretical Methods outlined in Sec. III.

A. Distributions of horizontal wind speeds at different heights

PDFs of the wind speeds sampled for the two heights $h = 30$ m and $h = 90$ m (symbols) are displayed in Fig. 3(a) together with fits of the Weibull distribution to the data (solid lines). For the fitting, we applied the Levenberg-Marquardt algorithm [88]. The Weibull distribution gives a good description except in the tail regime where it underestimates the frequency of high horizontal wind speeds $u \gtrsim 18$ m/s. The deviation in the tail regime can be seen in the semilogarithmic representation in the inset in Fig. 3(a). The shape parameter k is close to two, in agreement with earlier studies reported in the literature [69, 89–91], see Fig. 3(b). The solid line in Fig. 3(b) indicates a weak logarithmic dependence of k on h ,

$$k(h) = k_0 - \alpha \ln \left(\frac{h}{h_0} \right), \quad (29)$$

where we have taken $h_0 = 30$ m as the reference height, $k_0 = k(h_0) \cong 2.0036$, and $\alpha \cong 0.15$. The shape parameter λ decreases approximately linearly with k , see the inset of Fig. 3(c). This yields

$$\lambda(h) = \lambda_0 - \lambda_s [k(h) - k_0] = \lambda_0 + \alpha \lambda_s \ln(h/h_0) \quad (30)$$

for the h -dependence, where the coefficients are $\lambda_0 \cong 9.12$ m/s and $\lambda_s \cong 3.33$ m/s. The solid line in Fig. 3(c) marks the dependence on h according to Eq. (30).

The mean velocity \bar{u} and the turbulence intensity σ_u/\bar{u} are related to k and λ :

$$\bar{u}(h) = \Gamma \left(1 + \frac{1}{k} \right) \lambda \cong \frac{\sqrt{\pi}}{2} \left[\lambda_0 + \alpha \lambda_s \ln \left(\frac{h}{h_0} \right) \right], \quad (31)$$

$$\frac{\sigma_u}{\bar{u}} = \sqrt{\frac{\Gamma \left(1 + \frac{2}{k} \right)}{\Gamma^2 \left(1 + \frac{1}{k} \right)}} - 1 \cong \sqrt{\frac{4}{\pi}} - 1 \cong 0.52. \quad (32)$$

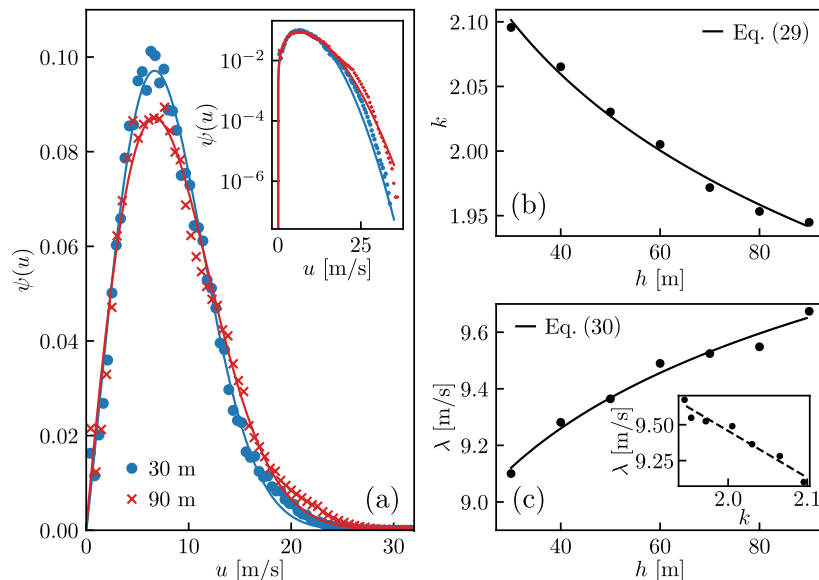


FIG. 3. (a) PDFs of wind speeds at heights 30 m (dots) and 90 m (crosses) and fits of Weibull distributions to the data [Eq. (1)] (solid lines). The fitting was carried out by using the Levenberg-Marquardt algorithm. The inset shows the PDFs together with the fits in the semi-logarithmic representation. (b) Shape parameters k (circles) and (c) scale parameters λ (circles) of the fitted Weibull distributions as a function of height h . The lines in (b) and (c) are least-square fits to Eqs. (29) and (30). The inset in (c) shows the λ - in relation to the k -values (circles) with the dashed line being a linear least-square fit to the data, cf. Eq. (30).

Here, we have evaluated the Gamma functions at $k = 2$ in the approximate expressions. In agreement with earlier findings [92, 93] and theories of wall turbulence [94, 95], Eq. (31) gives a logarithmic increase of the mean wind speed \bar{u} with height h .

Figure 4 shows how the dissimilarity between the wind speed PDFs, as quantified by the symmetrized Kullback-Leibler divergence $D_{\text{KL}}(h_0, h)$ [see Eq. (4)], increases with h/h_0 . Using Eqs. (29) and (30), we can express this dependence. To this end, $D_{\text{KL}}(h_0, h)$ in Eq. (4) is considered as a function of k , i.e. k_1, λ_1 in Eq. (4) become k_0, λ_0 , and k_2, λ_2 become $k, \lambda(k)$, with $\lambda(k)$ the linear function in Eq. (30). Since k varies only weakly with h , we can expand this function D_{KL} of k in a Taylor series around k_0 . Up to second order, we obtain ($D_{\text{KL}} = 0$ and $dD_{\text{KL}}/dk = 0$ for

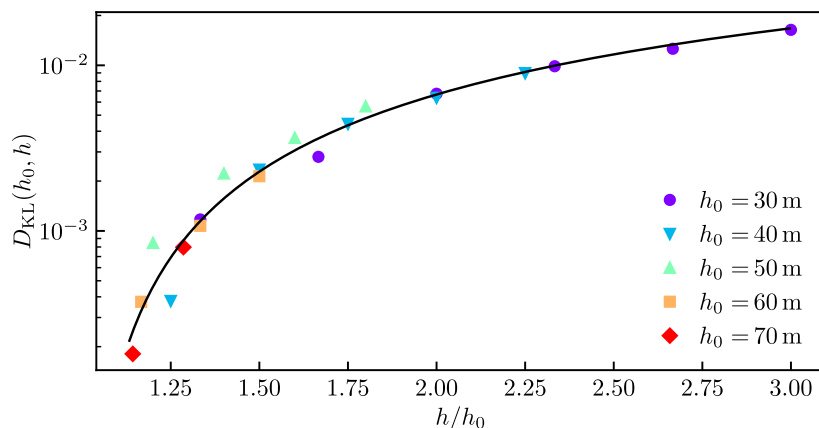


FIG. 4. Symmetrized Kullback-Leibler divergences $D_{\text{KL}}(h_0, h)$ [symbols, see Eq. (4)] as a function of h/h_0 . For k_1, k_2 and λ_1, λ_2 in Eq. (4), the parameters from the fits of the Weibull distributions in Figs. 3(b) and 3(c) are used. The solid line gives $D_{\text{KL}}(h_0, h)$ according to Eq. (33).

$k = k_0$),

$$\begin{aligned}
 D_{\text{KL}}(h_0, h) &= \frac{1}{2} \left[\left(1 - \gamma + \frac{\lambda_s}{\lambda_0} k_0^2 \right)^2 + \frac{\pi^2}{6} \right] \frac{\Delta k^2}{k_0^2} \\
 &= \frac{\alpha^2}{2k_0^2} \left[\left(1 - \gamma + \frac{\lambda_s}{\lambda_0} k_0^2 \right)^2 + \frac{\pi^2}{6} \right] \ln^2 \left(\frac{h}{h_0} \right).
 \end{aligned} \tag{33}$$

In the last step, we have inserted $\Delta k = -\alpha \ln(h/h_0)$ from Eq. (29). The solid line in Fig. 4 demonstrates that $D_{\text{KL}}(h_0, h)$ is well described by Eq. (33).

B. Temporal cross-correlations of wind speeds and wind speed increments at different heights

Kullback-Leibler divergences in the previous section quantify differences between distributions of the wind speeds, but do not allow conclusions regarding correlations. In this subsection, we discuss correlation properties of wind speeds, wind accelerations and wind speed increments.

Figure 5 shows the even parts $C_u^+(t; h_0, h_0 + \Delta h)$ (main graph) and odd parts $C_u^-(t; h_0, h_0 + \Delta h)$ (inset) of the correlation functions $C_u(t; h_0, h_0 + \Delta h)$ for a reference height $h_0 = 30$ m and different vertical separations Δh . The odd parts for $\Delta h \neq 0$ are negative and run through a minimum at values around $t \sim 10$ s. They are for all times much smaller than the even parts ($|C_u^-(t; h_0, h_0 + \Delta h)/C_u^+(t; h_0, h_0 + \Delta h)| < 2 \times 10^{-3}$), so that $C_u(t; h_0, h_0 + \Delta h) \simeq C_u^+(t; h_0, h_0 + \Delta h)$. For the even parts, we have plotted $1 - C_u^+(t; h_0, h_0 + \Delta h)$ rather than $C_u^+(t; h_0, h_0 + \Delta h)$ in the double-logarithmic representation to show that relative deviations between the cross-correlation functions for different Δh are strong at small times. For large times $t \gtrsim 10^4$ s, they become negligible. The $C_u^+(t; h_0, h_0 + \Delta h)$ decay very slowly, i.e. the curves in Fig. 5 slowly approach one for large t . The curve for $\Delta h = 0$ is proportional to the second-order structure function, $1 - C_u^+(t; h_0, h_0) = D_2(t, h_0)/2\sigma_u^2(h_0)$, where $D_2(t, h_0) = \langle u(t', h_0) - u(t' + t) \rangle_{t'}$.

Figure 6(a) shows the even parts $C_{\partial_t u}^+(t; h_0, h_0 + \Delta h)$ (main graph) and odd parts $C_{\partial_t u}^-(t; h_0, h_0 + \Delta h)$ (inset) of the correlation functions $C_{\partial_t u}(t; h_0, h_0 + \Delta h)$ for the same reference height $h_0 = 30$ m as in Fig. 5. The odd parts are negative for all t and run through a minimum at short times for $\Delta h \neq 0$. For the even part, we checked the relation (7) between $C_{\partial_t u}^+(t; h_0, h_0 + \Delta h)$ and $C_u^+(t; h_0, h_0 + \Delta h)$ and that the $C_{\partial_t u}^+(t; h_0, h_0 + \Delta h)$ satisfy the sum rule (8). The validity of Eq. (7) is demonstrated by the symbols in Fig. 5, which were determined by numerical calculations of the integral in Eq. (7). The confirmation of the relation (7) up to times $t \gtrsim 10^3$ s suggests that it holds true for all times and hence also the second sum rule (9). We could not verify it directly since the $C_{\partial_t u}^+(t; h_0, h_0 + \Delta h)$ do not have sufficient numerical accuracy for $t \gtrsim 10^3$ s.

The autocorrelation function $C_{\partial_t u}^+(t; h_0, h_0)$ in Fig. 6(a) rapidly decreases from its value one at $t = 0$ to a negative

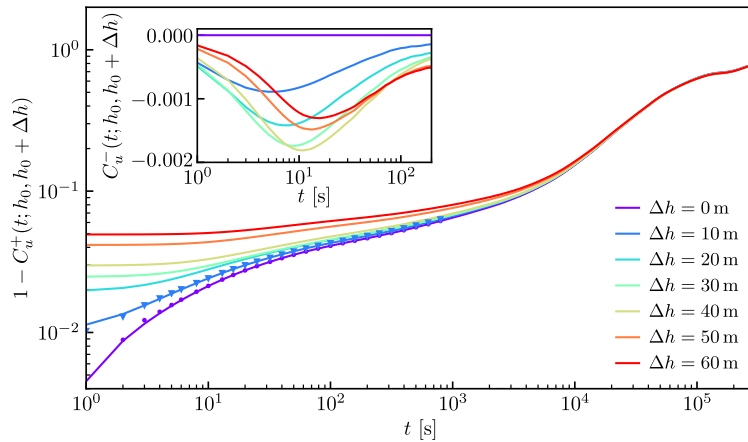


FIG. 5. Even parts $C_u^+(t; h_0, h_0 + \Delta h)$ of cross-correlation functions between wind speeds [solid lines, see Eq. (5)] for various height separations Δh from the reference height $h_0 = 30$ m. For better visibility of the relative deviations between the curves for different Δh , we have plotted $1 - C_u^+(t; h_0, h_0 + \Delta h)$. The symbols for $\Delta h = 0$ m and $\Delta h = 10$ m are obtained from Eq. (7), where the integral in this equation was calculated numerically. The inset shows the odd parts $C_u^-(t; h_0, h_0 + \Delta h)$ of the cross-correlation functions.

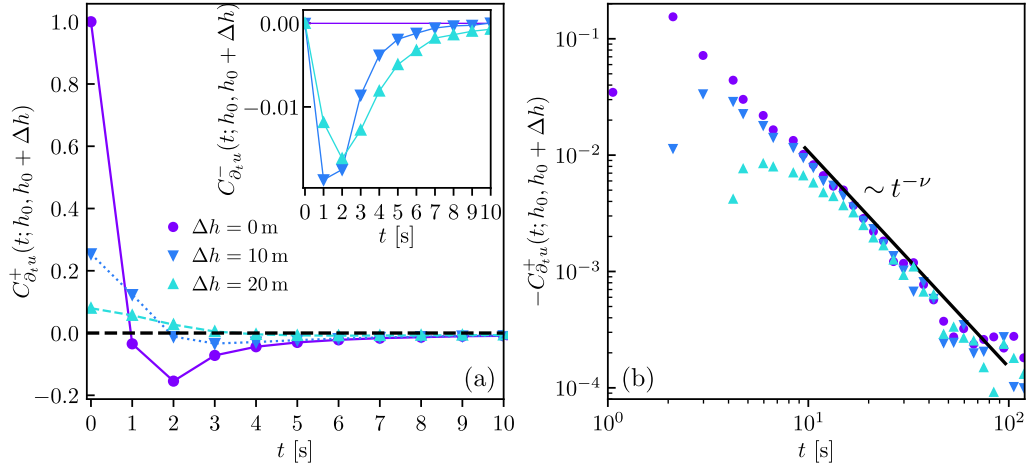


FIG. 6. (a) Even parts $C_{\partial_t u}^+(t; h_0, h_0 + \Delta h)$ of cross-correlation functions between time derivatives of wind speeds (symbols) at vertical separations $\Delta h = 0, 10, 20$ m from the reference height $h_0 = 30$ m. Lines are connecting the data as a guide for the eye. The inset shows the odd parts of the cross-correlation functions, including the autocorrelation analogous to Fig. 5. In (b), the even parts are shown in a double-logarithmic representation up to larger times. The solid line is a least-square fit of a power law to the autocorrelation data in the range $10 \text{ s} \leq t \leq 100 \text{ s}$, see Eq. (34).

minimal value and thereafter approaches zero smoothly. The functional form of $C_{\partial_t u}^+(t; h_0, h_0 + \Delta h)$ for $\Delta h > 0$ is similar, but $|C_{\partial_t u}^+(t; h_0, h_0 + \Delta h)|$ of the cross-correlations is reduced for small times $t \lesssim 7$ s compared to the autocorrelations. For larger times, relative deviations between the $C_{\partial_t u}^+(t; h_0, h_0 + \Delta h)$ for different Δh are insignificant, as Fig. 6(b) illustrates. The double-logarithmic plot suggests that the decay in the time regime $10 \text{ s} \lesssim t \lesssim 10^2 \text{ s}$ can be described by a power law,

$$C_{\partial_t u}^+(t; h_0, h_0 + \Delta h) \sim -A t^{-\nu}, \quad (34)$$

where $A \cong 0.7$ and $\nu \cong 1.9$.

Figure 7(a) shows the Pearson correlation coefficients $\rho(\tau; h_0, h_0 + \Delta h)$ defined in Eq. (14) as a function of Δh for various time lags τ and the same reference height $h_0 = 30$ m as in Figs. 5 and 6. The coefficients quantify how wind speed increments $\Delta_\tau u$ at vertical separation Δh are correlated. In all cases, the data can be well fitted by an exponential decay,

$$\rho(\tau; h_0, h_0 + \Delta h) = \exp\left[-\frac{\Delta h}{\xi(\tau)}\right], \quad (35)$$

where $\xi(\tau)$ is a τ -dependent correlation length.

The correlation length ξ increases with τ , see Fig. 7(b). For τ -scales corresponding to the regime of 3D isotropic turbulence (see Introduction), $\xi(\tau)$ is of the order of 10 m, i.e. smaller than the measurement heights h . For $\tau \gtrsim 10^5$ s, ξ approaches 1 km, which is comparable to the planetary boundary layer height [96]. This height is the upper limit, where vertical convection has a significant influence on the spatial distribution of horizontal wind speeds.

Interestingly, the variation of ξ with τ is similar to that of $1/\kappa(\tau, h)$ for fixed h , where $\kappa(\tau, h)$ is the kurtosis of the wind speed increment distribution at height h , $\kappa(\tau, h) = \langle \Delta_\tau u^4(t, h) \rangle_t / \langle \Delta_\tau u^2(t, h) \rangle_t^2$. We have included the plot of $1/\kappa(\tau, h_0)$ as a function of τ in Fig. 7(b) for the reference height $h_0 = 30$ m. For other h , the corresponding curve would look almost the same, i.e. there are no significant changes in the dependence of $1/\kappa(\tau, h)$ on τ when varying h . The similarity in the behavior of $\xi(\tau)$ and $1/\kappa(\tau, h)$ can be interpreted as follows: when $\kappa(\tau, h)$ is large, the probability for the occurrence of very large wind speed increments is high. Large wind speed increments disturb coherent turbulent structures and hence spatial correlations. Accordingly, one can expect ξ to become smaller for larger κ in agreement with the behavior seen in Fig. 7(b).

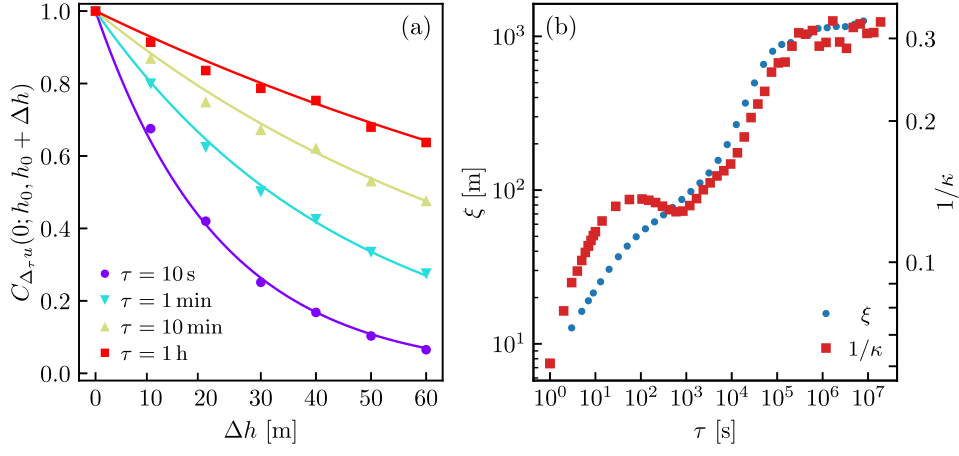


FIG. 7. (a) Pearson correlation coefficients between horizontal wind speed increments [symbols, see Eq. (14)] as a function of height difference Δh for various increment time lags τ and reference height $h_0 = 30$ m. Solid lines are least-square fits to Eq. (35). (b) Correlation lengths ξ obtained from the fits (circles) and inverse kurtosis $1/\kappa$ of the increment distributions (squares) as a function of τ .

C. Detrended fluctuation analysis of differences between wind speeds in vertical direction

A representative example of a one-hour section of the time series of wind speed differences $\Delta u_{h_1, h_2}(t) = u(t, h_1) - u(t, h_2)$ for heights $h_1 = 40$ m and $h_2 = 50$ m is shown in Fig. 8(a). The patchy structure of this series suggests the presence of long-time correlations [75]. In Fig. 8(b), we display profiles $R_{h_1, h_2}(t)$ of the detrended random walk calculated from Eq. (16) for the time window in Fig. 8(a). The black line corresponds to the data in Fig. 8(a) [$h_1 = 40$ m, $h_2 = 50$ m]. Two further profiles for heights $h_1 = 50$ m, $h_2 = 60$ m (red) and $h_1 = 50$ m, $h_2 = 80$ m (blue) are shown also.

Fluctuation functions $F_{h_1, h_2}(t)$ calculated from the profiles, see Eq. (18), are depicted in Fig. 9 for $h_1 = 50$ m, and $h_2 = 40$ m, 60 m, and 80 m. One can identify two regimes, separated by a crossover time $t_\times \simeq 110$ s, where $F(t)$ shows different power-law behavior. In the long-time regime $t > t_\times$, fluctuation functions scale as $F(t) \sim t^{H_1}$, with a Hurst exponent $H_1 \simeq 0.96$ showing no significant variation with heights h_1, h_2 . In the short-time regime, $t < t_\times$, $F(t) \sim t^{H_s}$, where the Hurst exponent H_s is smaller than H_1 and depends on h_1 and h_2 . The values vary in the range

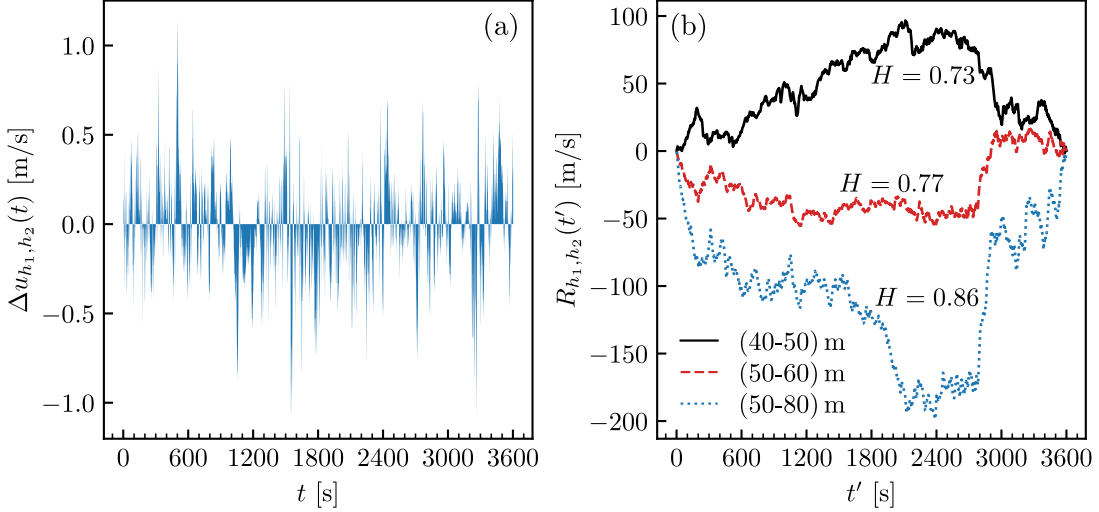


FIG. 8. (a) One-hour section of the time series of wind speed differences $\Delta u_{h_1, h_2}(t) = u(t, h_1) - u(t, h_2)$ at heights $h_1 = 40$ m and $h_2 = 50$ m. (b) Profile $R_{h_1, h_2}(t')$ of the detrended random walk in the one-hour time window generated from the data in (a) according to Eq. (16) (black). Two further profiles in the same one-hour time window are shown for heights $h_1 = 50$ m, $h_2 = 60$ m (red) and $h_1 = 50$ m, $h_2 = 80$ m (blue).

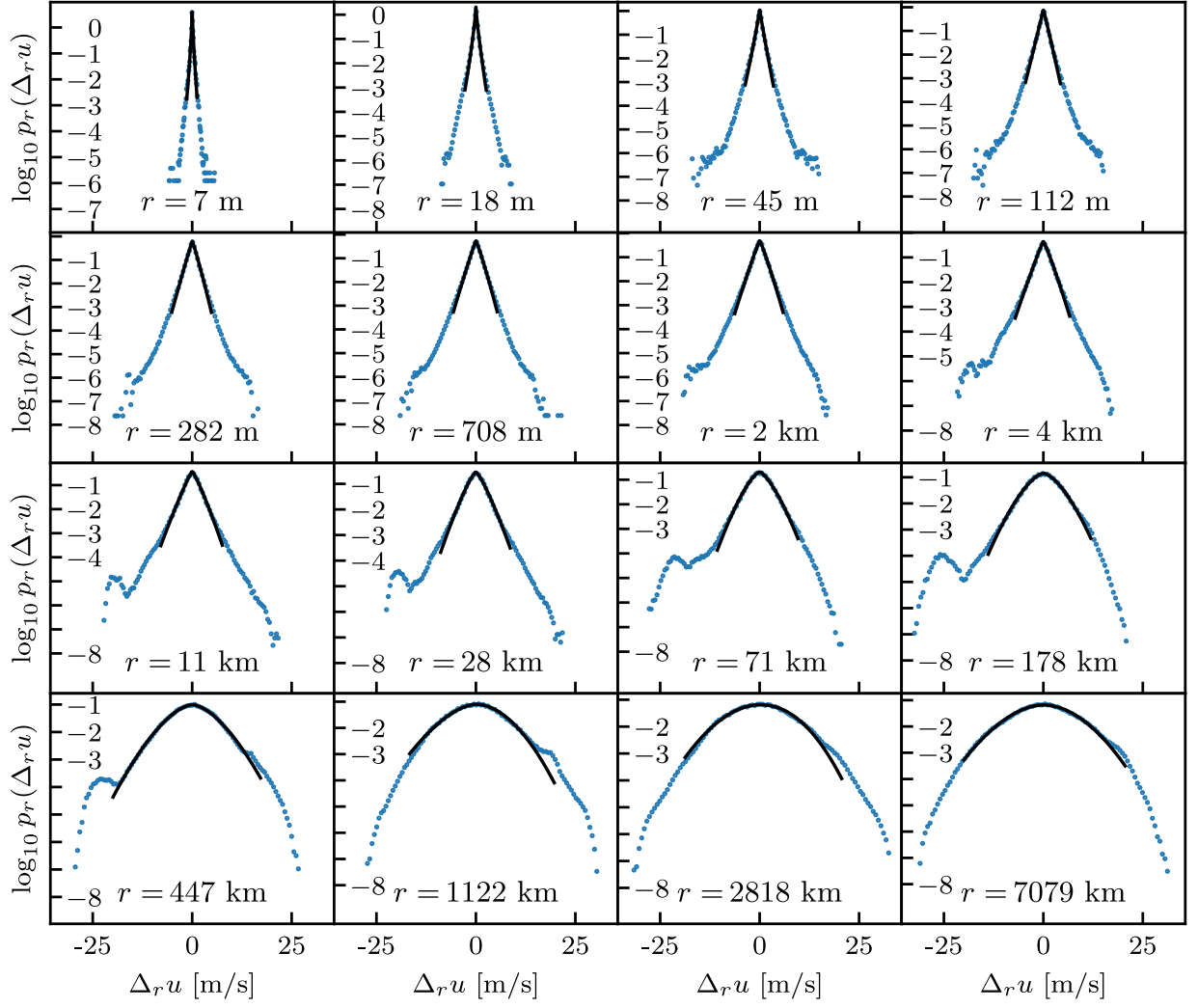


FIG. 10. PDFs $p_r(\Delta_r u)$ of horizontal wind speed increments $\Delta_r u$ for 16 different Taylor distances r at height $h = 90$ m. The black lines indicate least-square fits of the data to Eq. (37) in the core part $[\Delta_r u^-, \Delta_r u^+]$, where $\Delta_r u^-$ and $\Delta_r u^+$ are the first and last g -quantiles for $g = 10^3$, see Eq. (36).

skewed stretched exponential functions,

$$p_r(\Delta_r u) \propto \begin{cases} \exp\{-|\Delta_r u/s_-|^{\alpha_-}\}, & \Delta_r u \leq 0, \\ \exp\{-|\Delta_r u/s_+|^{\alpha_+}\}, & \Delta_r u > 0, \end{cases} \quad (37)$$

where the scale parameters s_{\pm} quantify the widths and the shape parameters α_{\pm} describe the decays for negative and positive $\Delta_r u$, respectively. Corresponding least-square fits are shown as solid lines in Fig. 10.

In Fig. 11, we display the fit parameters for $h = 90$ m, and in the insets the parameters for $h = 30$ m. For both $h = 30$ m and 90 m, the parameters are nearly the same, demonstrating that the core part of the wind speed increment PDFs is almost independent of h . The scale parameters s_{\pm} in Fig. 11(a) increase with r , reflecting the broadening of the PDFs in Fig. 10.

This broadening can also be quantified by the second-order structure functions $D_2(r)$, see Eq. (20). In fact, by assuming Eq. (37) to describe the PDFs for all $\Delta_r u$, one finds

$$D_2 = a^2(s_-^2 + b^2 s_+^2), \quad (38)$$

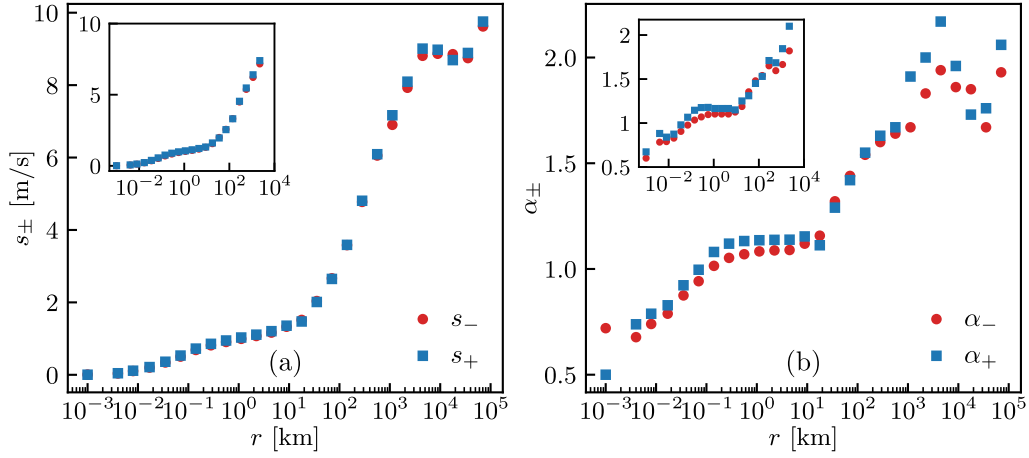


FIG. 11. (a) Scale parameters s_{\pm} and (b) shape parameters α_{\pm} specifying the core part of the distribution of horizontal wind speed increments according to Eq. (37) (see also solid lines in Fig. 10). Data in the main figure parts are for height $h = 90$ m and in the insets for $h = 30$ m.

where

$$b^2 = \frac{\alpha_+ \Gamma(2/\alpha_-)}{\alpha_- \Gamma(2/\alpha_+)} \simeq 1,$$

and

$$a^2 = \frac{b^2 \frac{\Gamma(1/\alpha_+)}{\alpha_+} + \frac{\Gamma(1/\alpha_-)}{\alpha_-}}{b^2 \frac{\Gamma(3/\alpha_+)}{\alpha_+} + \frac{\Gamma(3/\alpha_-)}{\alpha_-}}.$$

The shape parameters α_{\pm} in Fig. 11(b) increase from values $\alpha_{\pm} < 1$ for small r , to values $\alpha_{\pm} \simeq 2$ for large r . Accordingly, deviations from a Gaussian distribution become less pronounced for larger distances r , as it can be seen also by the change of shape of the core part from tent-like to parabolic in Fig. 10.

In addition to the features describing the core part of the distributions, bumps occur in both the left and right tail of the PDFs in Fig. 10, see, for example, the results for $r = 4$ km and $r = 1122$ km. The bumps in the right tail appear for $r \gtrsim 400$ km and are small. The bumps in the left tail become more pronounced with increasing r and develop into a peak around $\Delta_r u \simeq -25$ m/s, see the PDFs in the range 10 km $< r < 450$ km. When the Taylor distance changes from $r = 447$ km to $r = 1122$ km, the peak suddenly disappears.

Interestingly, the second peak at negative $\Delta_r u$ has a strong impact on the change of sign in the third-order structure function $D_3(r)$ and its scaling behavior in the regime 10-200 km. This is demonstrated in Fig. 12, where in (a), $D_3(r)$ is plotted for the core part, assuming Eq. (37) to provide a description for all $\Delta_r u$, while in Fig. 12(b), D_3 was calculated for all data including the bumps in the tails of the PDF. In both Figs. 12(a) and (b), D_3 changes sign, but in Fig. 12(a) this change occurs at a significantly smaller $r \simeq 100$ km, compared to $r \simeq 500$ km in Fig. 12(b). In view of previous results reported in the literature [4, 55, 77, 100, 101], the value $r \simeq 500$ km is more reliable, indicating that the tail features of the PDF have a decisive influence.

This finding is further corroborated when analyzing the scaling behavior of D_3 , where $D_3 = -2\epsilon r$ is expected for the regime of 3D turbulence induced by gravity waves [Eq. (22)], and $D_3 = \eta r^3/4$ for the regime of geostrophic turbulence [Eq. (23)], see also Fig. 1. In the insets of Figs. 12(a) and (b), $D_3(r)$ is plotted in double-logarithmic representation. For the 3D turbulence regime induced by gravity waves, the expected scaling $D_3 \sim -r$ is clearly visible in the inset of Fig. 12(b), while it cannot be seen in the inset of Fig. 12(a). The solid lines with slopes three indicate a scaling $D_3 \sim r^3$ as it is expected in the regime of geostrophic turbulence. The D_3 from our analysis show a strong rise in the respective r regime, which may reflect such scaling behavior. Due to the small range of the regime and the scatter of the D_3 data in it, however, one cannot speak about an agreement with theoretical predictions.

We denote the wind speed increments, where $p_r(\Delta u)$ exhibits a local minimum and maximum in its left tail as $(\Delta_r u)_{\max}$ and $(\Delta_r u)_{\min}$, see the inset of Fig. 13(a). How $(\Delta_r u)_{\max}$ varies with the Taylor distance r for various heights h is shown in Fig. 13(a). With increasing h , $(\Delta_r u)_{\max}$ decreases, i.e. the position of the second peak shifts further into the left tail part of $p_r(\Delta_r u)$. For all h , $(\Delta_r u)_{\max}$ becomes minimal at a Taylor distance of about 250 km.

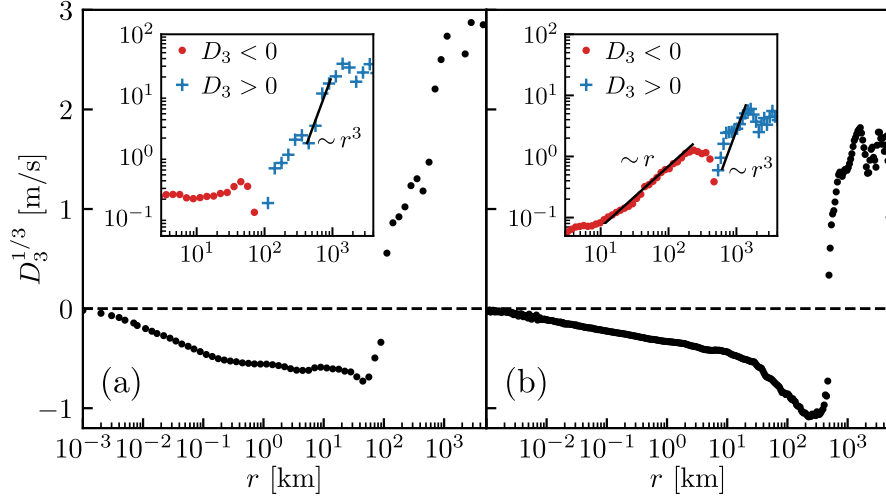


FIG. 12. Third-order structure function at height $h = 90$ m as a function of the Taylor distance r for (a) the core part of the distribution of horizontal wind speed increments [PDFs given by Eqs. (37)], and (b) the full PDFs. To make changes more clearly visible, the third root $D_3^{1/3}$ is plotted. The insets show the third-structure function in a double-logarithmic representation, where red circles indicate $-D_3$ (sign conversion for negative D_3) and blue crosses $+D_3$ (no sign conversion). In the interval 500 – 1000 km, the solid lines in the insets have slope three according to the scaling behavior $D_3(r) \sim r^3$ predicted by theory for geostrophic turbulence, see Eq. (23) and Fig. 1. In the inset in (b), a second solid line in the interval 10 – 200 km has slope one according to the scaling, $D_3(r) \sim -r$ predicted for 3D turbulence induced by gravity waves, see Eq. (22).

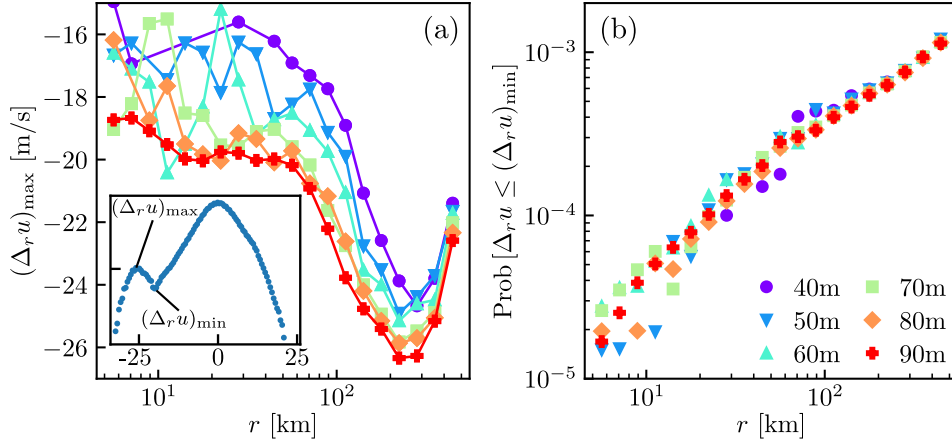


FIG. 13. (a) Horizontal wind speed increments $(\Delta_r u)_{\max}$, where $p_r(\Delta_r u)$ shows a local maximum in its left tail, see the example in the inset, where $p_r(\Delta_r u)$ is shown for $h = 90$ m and $r = 178$ km; for further examples, see Fig. 10. Also indicated in the inset is the increment $(\Delta_r u)_{\min}$, where $p_r(\Delta_r u)$ has a minimum. (b) Probability of finding a speed increment $\Delta_r u < (\Delta_r u)_{\min}$. Data in (a) and (b) are shown for six different heights. Assignment of symbols and color coding are given in the legend in (b).

Interestingly, this value coincides with the minimum of the third-order structure function D_3 , see Fig. 12(b).

The data suggest that increments $\Delta u_r < (\Delta_r u)_{\min}$ are resulting from a different physical mechanism than increments $\Delta u_r > (\Delta_r u)_{\min}$ distributed according to the core part of $p_r(u)$. The probability $\text{Prob}[\Delta_r u \leq (\Delta_r u)_{\min}]$ for increments $\Delta u_r < (\Delta_r u)_{\min}$ to occur, is depicted in Fig. 13(b). It increases approximately linearly with r .

To summarize, our analysis indicates that the peak in the left tail of distributions of horizontal wind speed increments is decisive to obtain the scaling features of $D_3(r)$ according to gravity-wave induced turbulence, Eq. (22). The distance, at which this peak appears at largest negative speed increments $(\Delta_r u)_{\max}$, agrees with the minimum of $D_3(r)$. We have checked also that the peak appears robustly when bootstrapping the data by determining increment PDFs for ten separate chunks of two months. These findings suggest that the peak in the left tail is not an artifact but an important, so-far unexplored feature. That it was not reported yet, could be due to the lack of sufficient amount of data for resolving it in the tail part of PDFs.

E. Scaling behavior of moments of horizontal wind speed increment distributions

For Taylor distances $r \lesssim h$, i.e. in the inertial regime of 3D isotropic turbulence, intermittency shows up in large values of wind speed increments that are much more frequent than expected from Gaussian statistics. The intermittency is reflected in multifractal behavior, given by the nonlinear q -dependence of exponents $\zeta(q)$ in Eq. (25). Figure 14 shows \tilde{D}_q as function of (a) r and (b) $\tilde{D}_3(r)$ [ESS analysis] for the measurement height $h = 90$ m and various orders q . The solid lines in the figures are least-square fits of power laws to the data in the inertial regime. In agreement with results reported earlier in the literature [30], the range of the power-law behavior in the ESS analysis extends, corresponding to distances $r \gtrsim h$ [Fig. 14(b)].

The slopes of the lines in the double-logarithmic plots yield the exponents $\zeta(q)$, see Eqs. (25) and (26). They are shown in Fig. 14(c). At small q , the exponents approximately follow the linear monofractal behavior $\zeta(q) = q/3$ according to K41 scaling, which is indicated by the straight solid blue line. At larger q , the concave curvature of the $\zeta(q)$ signatures nonlinear multifractal behavior due to intermittency corrections. The theoretical prediction (28) [SL] describes quite closely the exponents $\zeta(q)$ obtained from power-law scaling of \tilde{D}_q with r . However, neither of the Eqs. (27) [K61] and (28) [SL] gives $\zeta(q)$ accurately.

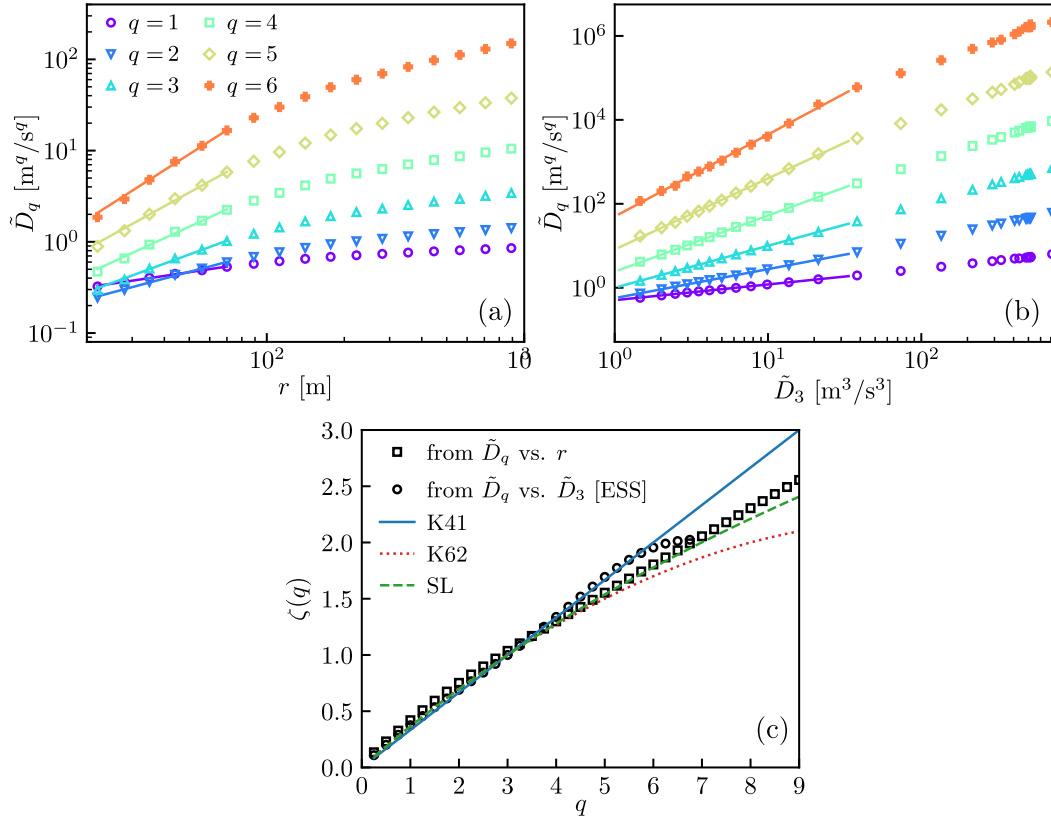


FIG. 14. (a, b) Structure functions \tilde{D}_q (symbols) for absolute values of wind speed differences [see Eq. (24)] for height $h = 90$ m as a function of (a) r and (b) $\tilde{D}_3(r)$. The solid lines are least-square fits to a power-law behavior in the inertial regime of 3D isotropic turbulence, see Eqs. (25) and (26). (c) Exponents $\zeta(q)$ obtained from the power-law fits in (a) and (b). The dashed blue line referenced as K41 indicates a monofractal behavior with the exponent $\zeta(q) = q/3$, which applies when assuming a self-similar structure of the turbulent wind field [58]. The red solid line indicates the nonlinear multifractal behavior of $\zeta(q)$ according to Eqs. (27) with $\mu = 0.45$, referenced as K62. The green solid line refers to the nonlinear multifractal behavior according to Eq. (28), referenced as SL.

V. CONCLUSIONS

We have analyzed offshore horizontal wind speeds sampled in the North Sea at heights 30 – 90 m above the sea level over a time period of 20 months with a time resolution of one second. Distributions and correlation properties were investigated for wind speeds and wind speed increments. Cross-correlation functions were determined with respect to time and height differences. For equal-time wind speed differences at different heights, we carried out a detrended fluctuation analysis. In the analysis of distributions of wind speed increments and their moments, we considered a mapping of time lags τ onto spatial distances r by applying the Taylor’s hypothesis locally, i.e. by using the mean wind speed \bar{u}_τ in every time window given by the lag τ . We call the resulting $r = \bar{u}_\tau \tau$ Taylor distance.

Distributions of horizontal wind speeds can be described by the Weibull form. This form, however, underestimates the frequency of high wind speeds $\gtrsim 18$ m/s in the tail region. Both the shape parameter k and the scale parameter λ of the Weibull distribution vary weakly with the height h above the sea level. The shape parameter k is about two and decreases logarithmically with h . The scale parameter λ decreases approximately linearly with k . These results yield a height-independent turbulence intensity of about one half and a logarithmic increase of the mean wind speed with h , in agreement with previously reported findings and theories of wall turbulence. As a measure of the differences between wind speed distributions at different heights, we calculated the symmetrized Kullback-Leibler divergence. It increases as $\sim \ln^2(h/h_0)$ with h , where h_0 is a reference height.

Cross-correlation functions between wind speeds at different heights decay very slowly. Relative deviations between them are significant for small times, while for large times $t \gtrsim 10^4$ s they are almost equal. A detrended fluctuation analysis of differences between equal-time wind speeds at different heights showed a short- and long-time scaling regime with Hurst exponents of about 0.75 and close to one. These large Hurst exponents reflect strong persistent correlations in the temporal changes of equal-time wind speed differences.

Cross-correlation functions between time derivatives $\partial_t u(t, h)$ of wind speeds, numerically represented by wind speed increments in the smallest time interval $\Delta t = 1$ s, show anticorrelations. They slowly decay towards zero from negative values. At short times, cross-correlations between $\partial_t u(t, h)$ and $\partial_t u(t, h + \Delta h)$ quickly drop to negative values and their magnitudes become much smaller for larger height differences Δh . For larger times $t \gtrsim 10^2$ s, no significant variation with the vertical separation Δh occurs. Both the auto- and the even parts of cross-correlation functions satisfy sum rules required by the fact that the mean kinetic wind energy should not diverge, i.e. by the finite variance of wind speed distributions. Equal-time correlations between wind speed increments of time lag τ at different heights decay exponentially with the height separation Δh , where the correlation length ξ of the exponential decay increases monotonically with τ .

Moments of the distribution of wind speed increments show intermittency corrections in the regime of 3D isotropic turbulence. The intermittency is reflected in a multifractal scaling behavior of the moments with the Taylor distance. Models suggested for the multifractal scaling give an approximate but not perfect match to the data.

Distributions of wind speed increments $\Delta_r u$ at Taylor distances r have a tent-like shape in the core part around $\Delta_r u$ for small r . With increasing r , their shape in the core part changes and approaches a Gaussian for large $r \gtrsim 10^3$ km.

A striking feature in the distribution of wind speed increments is the occurrence of a peak in their left tails for Taylor distances in the range 10 – 200 km. In this regime, turbulent wind fields are commonly believed to be governed by gravity waves. Interestingly, the expected and observed linear scaling $D_3(r) \sim -r$ of the third-order structure breaks down in this regime, when the peak in the left tails is ignored, i.e. when using the shape of the core part to represent the full distributions including their tails. This suggests that the peak is an intrinsic feature of atmospheric turbulence. It will be interesting to see whether further investigations can corroborate or confirm this finding.

An open question concerns the dependence of our findings on varying stratification conditions. In a recent combined analysis of airborne and stationary measurements at the FINO1 mast [67], atmospheric stability was found to depend on the measurement height h , where predominantly stable conditions were reported for $55 \text{ m} < h < 95 \text{ m}$. For quantifying atmospheric stability, suitable criteria need to be considered based on, for example, the lapse rate, the bulk Richardson number, and the Monin-Obukhov parameter [102]. Evaluation of these parameters requires to include additional information about temperature and pressure profiles, air humidity and vertical wind velocities in the analysis, which is beyond the scope of this study.

Our present analysis of offshore wind speed data allows for testing theoretical approaches against empirical findings and thus lays a suitable basis to benchmark data obtained from stochastic wind speed modeling.

ACKNOWLEDGMENTS

We thank J. Peinke for valuable discussions and M. Wächter for helping us with the data acquisition. We are grateful to the BMWI (Bundesministerium für Wirtschaft und Energie) and the PTJ (Projektträger Jülich) for providing the data of the offshore measurements at the FINO1 platform. We acknowledge use of a high-performance computing

cluster funded by the Deutsche Forschungsgemeinschaft (Project No. 456666331).

-
- [1] I. Suomi and T. Vihma, Wind gust measurement techniques - from traditional anemometry to new possibilities, *Sensors* **18**, 1300 (2018).
 - [2] J. G. V. van Ramshorst, M. Coenders-Gerrits, B. Schilperoort, B. J. H. van de Wiel, J. G. Izett, J. S. Selker, C. W. Higgins, H. H. G. Savenije, and N. C. van de Giesen, Revisiting wind speed measurements using actively heated fiber optics: a wind tunnel study, *Atmos. Meas. Tech.* **13**, 5423 (2020).
 - [3] X. G. Larsén, S. E. Larsen, and E. L. Petersen, Full-scale spectrum of boundary-layer winds, *Boundary-Layer Meteorol.* **159**, 349 (2016).
 - [4] S.-K. Sim, J. Peinke, and P. Maass, Signatures of geostrophic turbulence in power spectra and third-order structure function of offshore wind speed fluctuations, *Sci. Rep.* **13**, 13411 (2023).
 - [5] P. Veers, K. Dykes, E. Lantz, S. Barth, C. L. Bottasso, O. Carlson, A. Clifton, J. Green, P. Green, H. Holttinen, D. Laird, V. Lehtomäki, J. K. Lundquist, J. Manwell, M. Marquis, C. Meneveau, P. Moriarty, X. Munduate, M. Muskulus, J. Naughton, L. Pao, J. Paquette, J. Peinke, A. Robertson, R. J. Sanz, A. M. Sempreviva, J. C. Smith, A. Tuohy, and R. Wisser, Grand challenges in the science of wind energy, *Science* **366**, eaau2027 (2019).
 - [6] Á. Leelőssy, F. Molnár Jr., F. Izsák, Á. Havasi, I. Lagzi, and R. Mészáros, Dispersion modeling of air pollutants in the atmosphere: a review, *Cent. Eur. J. Geosci. Open Geosciences*, **6**, 257 (2014).
 - [7] S. Tan and R. Ni, Universality and intermittency of pair dispersion in turbulence, *Phys. Rev. Lett.* **128**, 114502 (2022).
 - [8] A. Costa, A. Crespo, J. Navarro, G. Lizcano, H. Madsen, and E. Feitosa, A review on the young history of the wind power short-term prediction, *Renewable Sustainable Energy Rev.* **12**, 1725 (2008).
 - [9] M. Santhosh, C. Venkaiah, and D. M. Vinod Kumar, Current advances and approaches in wind speed and wind power forecasting for improved renewable energy integration: A review, *Eng. Rep.* **2**, e12178 (2020).
 - [10] S. Hanifi, X. Liu, Z. Lin, and S. Lotfian, A critical review of wind power forecasting methods – past, present and future, *Energies* **13**, 3764 (2020).
 - [11] R. Tawn and J. Browell, A review of very short-term wind and solar power forecasting, *Renewable Sustainable Energy Rev.* **153**, 111758 (2022).
 - [12] B. Sanderse, S. van der Pijl, and B. Koren, Review of computational fluid dynamics for wind turbine wake aerodynamics, *Wind Energy* **14**, 799 (2011).
 - [13] C. L. Archer, A. Vassel-Behagh, C. Yan, S. Wu, Y. Pan, J. F. Brodie, and A. E. Maguire, Review and evaluation of wake loss models for wind energy applications, *Appl. Energy* **226**, 1187 (2018).
 - [14] R. Nash, R. Nouri, and A. Vassel-Behagh, Wind turbine wake control strategies: A review and concept proposal, *Energy Convers. Manage.* **245**, 114581 (2021).
 - [15] D. R. Houck, Review of wake management techniques for wind turbines, *Wind Energy* **25**, 195 (2022).
 - [16] F. Porté-Agel, M. Bastankhah, and S. Shamsoddin, Wind-turbine and wind-farm flows: A review, *Boundary-Layer Meteorol.* **174**, 1 (2020).
 - [17] M. Bošnjaković, M. Katinić, R. Santa, and D. Marić, Wind turbine technology trends, *Appl. Sci.* **12**, 8653 (2022).
 - [18] G. Johnson, *Wind Energy Systems* (Prentice-Hall, Englewood Cliffs, 1998).
 - [19] I. Y. Lun and J. C. Lam, A study of weibull parameters using long-term wind observations, *Renewable Energy* **20**, 145 (2000).
 - [20] Z. R. Shu and M. Jesson, Estimation of Weibull parameters for wind energy analysis across the UK, *J. Renewable Sustainable Energy* **13**, 023303 (2021).
 - [21] B. Castaing, Y. Gagne, and E. J. Hopfinger, Velocity probability density functions of high Reynolds number turbulence, *Physica D* **46**, 177 (1990).
 - [22] F. Böttcher, S. Barth, and J. Peinke, Small and large scale fluctuations in atmospheric wind speeds, *Stochastic Environ. Res. Risk Assess.* **21**, 299 (2007).
 - [23] P. Milan, M. Wächter, and J. Peinke, Turbulent character of wind energy, *Phys. Rev. Lett.* **110**, 138701 (2013).
 - [24] A. N. Kolmogorov, A refinement of previous hypotheses concerning the local structure of turbulence in a viscous incompressible fluid at high Reynolds number, *J. Fluid Mech.* **13**, 82 (1962).
 - [25] E. Mollo-Christensen, Intermittency in large-scale turbulent flows, *Annu. Rev. Fluid Mech.* **5**, 101 (1973).
 - [26] D. Lohse and S. Grossmann, Intermittency in turbulence, *Physica A* **194**, 519 (1993).
 - [27] R. Benzi and A. Vulpiani, Multifractal approach to fully developed turbulence, *Rend. Lincei Sci. Fis. Nat.* **33**, 471 (2022).
 - [28] P. L. Johnson and M. Wilczek, Multiscale velocity gradients in turbulence, *Annu. Rev. Fluid Mech.* **56**, 463 (2024).
 - [29] Z.-S. She and E. Leveque, Universal scaling laws in fully developed turbulence, *Phys. Rev. Lett.* **72**, 336 (1994).
 - [30] R. Benzi, S. Ciliberto, R. Tripiccone, C. Baudet, F. Massaioli, and S. Succi, Extended self-similarity in turbulent flows, *Phys. Rev. E* **48**, R29 (1993).
 - [31] S. Grossmann, D. Lohse, and A. Reeh, Application of extended self-similarity in turbulence, *Phys. Rev. E* **56**, 5473 (1997).
 - [32] G. Amati, R. Benzi, and S. Succi, Extended self-similarity in boundary layer turbulence, *Phys. Rev. E* **55**, 6985 (1997).
 - [33] J. M. Vindel, C. Yagüe, and J. M. Redondo, Structure function analysis and intermittency in the atmospheric boundary layer, *Nonlin. Processes Geophys.* **15**, 915 (2008).
 - [34] V. P. Kiliyanpilakkil and S. Basu, Extended self-similarity of atmospheric boundary layer wind fields in mesoscale regime:

- Is it real?, *Europhys. Lett.* **112**, 64003 (2016).
- [35] R. Baile and J.-F. Muzy, Spatial intermittency of surface layer wind fluctuations at mesoscale range, *Phys. Rev. Lett.* **105**, 254501 (2010).
- [36] V. I. Nikora and D. G. Goring, Extended self-similarity in geophysical and geological applications, *Math. Geol.* **33**, 251 (2001).
- [37] V. K. Gupta and E. Waymire, Multiscaling properties of spatial rainfall and river flow distributions, *J. Geophys. Res.: Atmos.* **95**, 1999 (1990).
- [38] M. Schleiss, J. Jaffrain, and A. Berne, Statistical analysis of rainfall intermittency at small spatial and temporal scales, *Geophys. Res. Lett.* **38**, L18403 (2011).
- [39] V. Acuña, D. Jorda-Capdevila, P. Vezza, A. M. De Girolamo, M. E. McClain, R. Stubbington, A. V. Pastor, N. Lamouroux, D. von Schiller, A. Munné, and T. Datry, Accounting for flow intermittency in environmental flows design, *J. Appl. Ecol.* **57**, 742 (2020).
- [40] T. C. van Leth, H. Leijnse, A. Overeem, and R. Uijlenhoet, Rainfall spatiotemporal correlation and intermittency structure from micro- γ to meso- β scale in the netherlands, *J. Hydrometeorol.* **22**, 2227 (2021).
- [41] R. L. Wilby, C. W. Dawson, D. Yu, Z. Herring, A. Baruch, M. J. Ascott, D. L. Finney, D. M. J. Macdonald, J. H. Marsham, T. Matthews, and C. Murphy, Spatial and temporal scaling of sub-daily extreme rainfall for data sparse places, *Clim. Dyn.* **60**, 3577 (2023).
- [42] V. Yakhot, Mean-field approximation and extended self-similarity in turbulence, *Phys. Rev. Lett.* **87**, 234501 (2001).
- [43] A. C. Brett and S. E. Tuller, The autocorrelation of hourly wind speed observations, *J. Appl. Meteorol. Climatol.* **30**, 823 (1991).
- [44] G. Thomann and M. Barfield, The time variation of wind speeds and windfarm power output in Kansas, *IEEE Trans. Energy Convers.* **3**, 44 (1988).
- [45] I. A. Pérez, M. García, M. L. Sánchez, and B. de Torre, Autocorrelation analysis of meteorological data from a RASS sodar, *J. Appl. Meteorol.* **43**, 1213 (2004).
- [46] I. Eliasson, B. Offerle, C. Grimmond, and S. Lindqvist, Wind fields and turbulence statistics in an urban street canyon, *Atmos. Environ.* **40**, 1 (2006).
- [47] F. M. Ralph, P. J. Neiman, and D. Levinson, Lidar observations of a breaking mountain wave associated with extreme turbulence, *Geophys. Res. Lett.* **24**, 663 (1997).
- [48] G. I. Taylor, The spectrum of turbulence, *Proc. R. Soc. Lond. Ser. A* **164**, 476 (1938).
- [49] G. D. Nastrom and K. S. Gage, A first look at wavenumber spectra from gasp data, *Tellus A* **35A**, 383 (1983).
- [50] G. D. Nastrom, K. S. Gage, and W. H. Jasperson, Kinetic energy spectrum of large-and mesoscale atmospheric processes, *Nature* **310**, 36 (1984).
- [51] S. B. Pope, *Turbulent Flows* (Cambridge University Press, 2000).
- [52] U. Karban, E. Martini, P. Jordan, G. A. Brès, and A. Towne, Solutions to aliasing in time-resolved flow data, *Theor. Comput. Fluid Dyn.* **36**, 887 (2022).
- [53] J. G. Charney, Geostrophic turbulence, *J. Atmos. Sci.* **28**, 1087 (1971).
- [54] J.-H. Xie and O. Bühler, Exact third-order structure functions for two-dimensional turbulence, *J. Fluid Mech.* **851**, 672 (2018).
- [55] F. L. Poblet, J. Vierinen, V. Avsarkisov, J. F. Conte, H. Charuvil Asokan, C. Jacobi, and J. L. Chau, Horizontal correlation functions of wind fluctuations in the mesosphere and lower thermosphere, *J. Geophys. Res.: Atmos.* **128**, e2022JD038092 (2023).
- [56] M. Calaf, M. Hultmark, H. J. Oldroyd, V. Simeonov, and M. B. Parlange, Coherent structures and the k^{-1} spectral behaviour, *Phys. Fluids* **25**, 125107 (2013).
- [57] P. Drobinski, P. Carlotti, R. K. Newsom, R. M. Banta, R. C. Foster, and J.-L. Redelsperger, The structure of the near-neutral atmospheric surface layer, *J. Atmos. Sci.* **61**, 699 (2004).
- [58] A. N. Kolmogorov, The local structure of turbulence in incompressible viscous fluid for very large reynolds numbers, *Proc. R. Soc. London, Ser. A* **434**, 9 (1991).
- [59] A. R. Mehrens, A. N. Hahmann, X. G. Larsén, and L. von Bremen, Correlation and coherence of mesoscale wind speeds over the sea, *Q. J. R. Meteorolog. Soc.* **142**, 3186 (2016).
- [60] C. L. Vincent, X. G. Larsén, S. E. Larsen, and P. Sørensen, Cross-spectra over the sea from observations and mesoscale modelling, *Boundary-Layer Meteorol.* **146**, 297 (2013).
- [61] L. M. Bardal and L. R. Sætran, Spatial correlation of atmospheric wind at scales relevant for large scale wind turbines, *J. Phys. Conf. Ser.* **753**, 032033 (2016).
- [62] FINO1 project supported by the German Government through BMWi and PTJ. For further details on the data sampling and instrumentation, see <https://www.fino1.de/en>.
- [63] I. Karagali, M. Badger, A. N. Hahmann, A. Peña, C. B. Hasager, and A. M. Sempreviva, Spatial and temporal variability of winds in the Northern European Seas, *Renewable Energy* **57**, 200 (2013).
- [64] E. Deusebio, P. Augier, and E. Lindborg, Third-order structure functions in rotating and stratified turbulence: a comparison between numerical, analytical and observational results, *J. Fluid Mech.* **755**, 294 (2014).
- [65] A. Segalini and J. Arnqvist, A spectral model for stably stratified turbulence, *J. Fluid Mech.* **781**, 330 (2015).
- [66] H. Yassin and S. M. Griffies, Surface quasigeostrophic turbulence in variable stratification, *J. Phys. Oceanogr.* **52**, 2995 (2022).
- [67] A. Platis, M. Hundhausen, A. Lampert, S. Emeis, and J. Bange, The role of atmospheric stability and turbulence in offshore wind-farm wakes in the german bight, *Boundary-Layer Meteorol.* **182**, 441 (2022).

- [68] S. Tuller and A. Brett, The characteristics of wind velocity that favor the fitting of a weibull distribution in wind speed analysis, *J. Appl. Meteorol.* **23**, 124 (1984).
- [69] T. P. Chang, Performance comparison of six numerical methods in estimating weibull parameters for wind energy application, *Appl. Energy* **88**, 272 (2011).
- [70] K. Mohammadi, O. Alavi, A. Mostafaeipour, N. Goudarzi, and M. Jalilvand, Assessing different parameters estimation methods of weibull distribution to compute wind power density, *Energy Convers. Manage.* **108**, 322 (2016).
- [71] S.-K. Sim, P. Maass, and P. G. Lind, Wind speed modeling by nested ARIMA processes, *Energies* **12**, 69 (2019).
- [72] S. Kullback, *Information theory and statistics* (Courier Corporation, 1997).
- [73] R. Teixeira, A. O'Connor, and M. Nogal, Probabilistic sensitivity analysis of offshore wind turbines using a transformed kullback-leibler divergence, *Struct. Saf.* **81**, 101860 (2019).
- [74] A. Lapworth, The diurnal variation of the marine surface wind in an offshore flow, *Quart. J. R. Met. Soc.* **131**, 2367 (2005).
- [75] E. Koscielny-Bunde, A. Bunde, S. Havlin, H. E. Roman, Y. Goldreich, and H.-J. Schellnhuber, Indication of a universal persistence law governing atmospheric variability, *Phys. Rev. Lett.* **81**, 729 (1998).
- [76] G. E. Willis and J. W. Deardorff, On the use of Taylor's translation hypothesis for diffusion in the mixed layer, *Q. J. R. Meteorol. Soc.* **102**, 817 (1976).
- [77] J. Y. N. Cho and E. Lindborg, Horizontal velocity structure functions in the upper troposphere and lower stratosphere: 1. observations, *J. Geophys. Res.: Atmos.* **106**, 10223 (2001).
- [78] A. N. Kolmogorov, Dissipation of energy in the locally isotropic turbulence, *Proc. R. Soc. London, Ser. A* **434**, 15 (1991).
- [79] M. A. Taylor, S. Kurien, and G. L. Eyink, Recovering isotropic statistics in turbulence simulations: The kolmogorov 4/5th law, *Phys. Rev. E* **68**, 026310 (2003).
- [80] E. Lindborg and J. Y. N. Cho, Horizontal velocity structure functions in the upper troposphere and lower stratosphere: 2. Theoretical considerations, *J. Geophys. Res.: Atmos.* **106**, 10233 (2001).
- [81] E. Lindborg, Can the atmospheric kinetic energy spectrum be explained by two-dimensional turbulence?, *J. Fluid Mech.* **388**, 259 (1999).
- [82] E. Lindborg, Third-order structure function relations for quasi-geostrophic turbulence, *J. Fluid Mech.* **572**, 255 (2007).
- [83] F. L. Poblet, H. Liu, and J. L. Chau, Third-order structure functions of zonal winds in the thermosphere using champ and goce observations, *Geophys. Res. Lett.* **51**, e2024GL108367 (2024).
- [84] K. R. Sreenivasan and P. Kailasnath, An update on the intermittency exponent in turbulence, *Phys. Fluids A* **5**, 512 (1993).
- [85] A. Praskovskiy and S. Oncley, Comprehensive measurements of the intermittency exponent in high reynolds number turbulent flows, *Fluid Dyn. Res.* **21**, 331 (1997).
- [86] S. Lovejoy, D. Schertzer, and J. D. Stanway, Direct evidence of multifractal atmospheric cascades from planetary scales down to 1 km, *Phys. Rev. Lett.* **86**, 5200 (2001).
- [87] V. Yakhot, Probability density and scaling exponents of the moments of longitudinal velocity difference in strong turbulence, *Phys. Rev. E* **57**, 1737 (1998).
- [88] A. Fischer, A. F. Izmailov, and M. V. Solodov, The Levenberg–Marquardt method: an overview of modern convergence theories and more, *Comput. Optim. Appl.*, DOI:10.1007/s10589-024-00589-1 (2024).
- [89] P. A. Costa Rocha, R. C. de Sousa, C. F. de Andrade, and M. E. V. da Silva, Comparison of seven numerical methods for determining weibull parameters for wind energy generation in the northeast region of Brazil, *Appl. Energy* **89**, 395 (2012), special issue on Thermal Energy Management in the Process Industries.
- [90] I. Tizgui, F. El Guezar, H. Bouzahir, and B. Benaid, Comparison of methods in estimating weibull parameters for wind energy applications, *Int. J. Energy Sect. Manage.* **11**, 650 (2017).
- [91] H. Patidar, V. Shende, P. Baredar, and A. Soni, Comparative study of offshore wind energy potential assessment using different weibull parameters estimation methods, *Environ. Sci. Pollut. Res.* **29**, 46341 (2022).
- [92] S. Karlsson, The applicability of wind profile formulas to an urban-rural interface site, *Boundary-Layer Meteorol.* **34**, 333 (1986).
- [93] I. Marusic, J. P. Monty, M. Hultmark, and A. J. Smits, On the logarithmic region in wall turbulence, *J. Fluid Mech.* **716**, R3 (2013).
- [94] H. Tennekes, The logarithmic wind profile, *J. Atmos. Sci.* **30**, 234 (1973).
- [95] A. Townsend, *The structure of turbulent shear flow* (Cambridge University Press, 1976).
- [96] Y. Zhang, D. J. Seidel, and S. Zhang, Trends in planetary boundary layer height over Europe, *J. Clim.* **26**, 10071 (2013).
- [97] P. Tabeling, G. Zocchi, F. Belin, J. Maurer, and H. Willaime, Probability density functions, skewness, and flatness in large reynolds number turbulence, *Phys. Rev. E* **53**, 1613 (1996).
- [98] J. Peinke, S. Barth, F. Böttcher, D. Heinemann, and B. Lange, Turbulence, a challenging problem for wind energy, *Physica A* **338**, 187 (2004), proceedings of the conference A Nonlinear World: the Real World, 2nd International Conference on Frontier Science.
- [99] G. Ren, J. Wan, J. Liu, D. Yu, and L. Söder, Analysis of wind power intermittency based on historical wind power data, *Energy* **150**, 482 (2018).
- [100] E. Gkioulekas and K.-K. Tung, Recent developments in understanding two-dimensional turbulence and the nastrom–gale spectrum, *J. Low Temp. Phys.* **145**, 25 (2006).
- [101] J. Callies, R. Ferrari, and O. Bühler, Transition from geostrophic turbulence to inertia-gravity waves in the atmospheric energy spectrum, *Proc. Natl. Acad. Sci. U.S.A.* **111**, 17033 (2014).
- [102] R. B. Stull, ed., *An Introduction to Boundary Layer Meteorology* (Springer Dordrecht, 1988).